Nanoscale

PAPER

View Article Online
View Journal | View Issue

Cite this: *Nanoscale*, 2025, **17**, 20338

Dislocation-enabled plasticity in rutile TiO_{2-x} at room temperature

Bo Yang, *[a] Nicholas Richter, [a] Huan Li, [a] Zhongxia Shang,[a] Zihao He, [b] Hongyi Dou,[a] Jianan Shen, [a] R. Edwin García, [a] Noam Bernstein,[c] C. Stephen Hellberg, [c] Haiyan Wang [a,b] and Xinghang Zhang *[a]

Received 25th June 2025,
Accepted 1st August 2025

DOI: 10.1039/d5nr02684a

rsc.li/nanoscale

Ceramics are widely perceived as brittle. Recent research showed that the deformability of brittle ceramics can be improved by introducing defects, *e.g.*, dislocations and stacking faults, into the ceramics using flash sintering. However, many ceramic materials, including TiO_2, have limited room-temperature dislocation mobility. In this work, we explored a potential route to toughen ceramic materials by introducing oxygen vacancies into rutile TiO_2. Nanoindentation method was employed to investigate the deformation behavior of the oxygen-deficient TiO_{2-x}. Detailed post-deformation transmission electron microscopy analyses revealed a significant increase in dislocation density. The improved fracture toughness is attributed to the abundant dislocation plasticity in reduced TiO_2 with abundant oxygen vacancies. This study provides insight into understanding the influence of point defects and dislocations on the deformation behavior of ceramic materials towards the future designs of ductile ceramics at room temperature.

1 Introduction

Oxide materials widely employed in many industrial applications are known for their high strength but low fracture toughness. In contrast, in metallic materials, dislocations act as the primary plasticity carriers, allowing plastic deformation to occur without catastrophic failure.[1] Compared to metals, the dislocation density is often low in ceramic materials due to the prolonged high-temperature sintering process required for their densification.[2–4] In addition, dislocation nucleation and dislocation mobility are highly restricted due to their rigid ionic and covalent bonding and large Burgers vector.[2] The limited pre-existing dislocation population and the difficulty in dislocation nucleation during deformation lead to limited plasticity in ceramics. One method to alleviate this dilemma is by introducing pre-existing defects into ceramic materials. Numerous studies have shown that flash-sintered ceramics contain abundant dislocations.[5–11] Li *et al.* showed using the *in situ* micropillar compression technique in a scanning electron microscope that flash-sintered TiO_2 has substantial room-temperature plasticity.[11] Porz *et al.* demonstrated that an enhancement in fracture toughness in both single crystalline and polycrystalline $SrTiO_3$ can be achieved by the introduction of high-density pre-existing dislocations ($\rho_{disl} > 10^{14}$ m^{-2}).[4] Another factor contributing to this toughening behavior is the room temperature dislocation mobility in $SrTiO_3$. The introduction of high-density pre-existing dislocations allows dislocations to move at a shear stress as low as 60 MPa without the necessity to reach 17 GPa in the case of dislocation nucleation.[4,12] This phenomenon can potentially be replicated in many other ceramic systems with perovskites, wurtzite, and sphalerite structures to enable room-temperature dislocation mobility.[2,4,12,13] As a result, most explorations of dislocation-based ceramic plasticity have focused on the aforementioned categories.[14–16] The introduction of dislocations is typically achieved by severe mechanical deformation.[4,14,15,17]

The recent progress in the rapid densification of ceramics using flash sintering has led to the ability to introduce multiple classes of defects such as oxygen vacancies,[18–22] dislocations,[6–10] planar faults,[8,11,23] and secondary phases.[21,24] Extensive microscale deformation studies have revealed that the pre-existing defects introduced during the rapid densification process can effectively enhance the deformability of ceramic materials even at room temperature.[9–11] Intriguingly, ceramic materials such as rutile TiO_2, which were previously believed to have very limited dislocation mobility at room temperature, exhibit enhanced deformability after flash sintering.[2,11,25] In flash-sintered oxides, another important type of defect besides dislocation is point defects, such as oxygen vacancies, which are formed through the electrochemical reduction reaction.[18,19,24,26–29] Previous investigations on oxygen-deficient TiO_2 suggest that oxygen vacancies

[a]*School of Materials Engineering, Purdue University, West Lafayette, IN 47907, USA. E-mail: boyang837@gmail.com, xzhang98@purdue.edu*
[b]*School of Electrical and Computer Engineering, Purdue University, West Lafayette, IN 47907, USA*
[c]*U.S. Naval Research Laboratory, Washington, District of Columbia, USA*

can potentially reduce the critical resolved shear stress (τ_{CRSS}) in TiO_2 and lead to higher hardness owing to work-hardening compared to its stoichiometric counterpart.[30–32] A similar effect in reducing shear stress due to oxygen vacancy was recently reported by Stich *et al.* on single crystalline $SrTiO_3$.[33] However, to date, systematic investigation on the deformation behavior of oxygen-deficient ceramic materials is still lacking, which is essential for the exploration of defect-enabled plasticity in ceramic materials.

Rutile TiO_2 is chosen here as the model system for investigating the influence of oxygen vacancy on the deformation behavior because of the following considerations: (1) TiO_2 and its substoichiometric forms are technologically important materials serving in broad fields including microelectronics,[34–37] photocatalysis,[38–42] batteries,[43–45] and photovoltaics.[46] (2) Oxygen vacancy is one of the key defects in many of the aforementioned applications.[36–38,47] (3) The influence of oxygen vacancy on the lattice structure of TiO_2 has been well studied.[48–52] (4) There are limited studies on the deformation behavior of rutile TiO_2.[30–32,53] Understanding the deformation behavior of TiO_2, especially under the influence of oxygen vacancies, is essential because mechanical stress often occurs during the fabrication, integration, or operation of devices in real-world applications.[4] For instance, in microelectronics and battery electrodes, stress-induced deformation can lead to cracking, delamination, or performance degradation.[10,11] Oxygen vacancies not only affect the electrical and catalytic properties of TiO_2, but may also influence its dislocation motion and plasticity.[15] Therefore, studying the mechanical response of oxygen-deficient TiO_2 provides valuable insights into its structural stability and reliability in service environments.[17] The solubility limit of O vacancy in rutile TiO_{2-x} is $x \approx 0.005$.[49] Before the concentration of O vacancy reaches the solubility limit, the rutile lattice initially expands due to the transformation of Ti^{4+} ions to Ti^{3+} ions and increase in the Ti–O bond length.[48]

After the oxygen concentration exceeds the solubility limit, oxygen vacancies coalesce and form crystallographic shear planes (CSP) locally, leading to contraction of the lattice parameters.[48,52,54] The primary slip system for rutile TiO_2 is $\{10\bar{1}\}\langle 101\rangle$ and occasionally $\{110\}[001]$.[32] The previous literature has shown the strong correlation of pop-in events with the pressure–displacement (P–h) curves from nanoindentation experiments in ceramic materials. One of the concerns for using pop-in events to investigate the slip occurrence in ceramics is that they can also be caused by crack formation.[55] Therefore, the calculated τ_{CRSS} for a specimen under each condition has to be compared to the theoretical shear strength (τ_{th}) of the material, which can be estimated as follow:[55]

$$\tau_{th} \approx \frac{G}{2\pi} \approx \frac{E}{16} \quad (1)$$

where G and E are the shear modulus and Young's modulus of the crystal, respectively, which can be measured by nanoindentation experiments.

In this work, a (001) rutile TiO_2 single crystal was used to investigate the deformation behavior of a crystal with two levels of oxygen deficiency. The employment of a single crystal grown by the floating zone method with the typical $\rho_{disl} < 10^{10}$ m^{-2} (ref. 4) combined with annealing before treatment rules out the effect of pre-existing dislocations in the crystals. The mechanical strength and toughness of TiO_2 can be tailored by varying the O stoichiometry. This study provides insights into a potential method to toughen brittle ceramic materials through defect engineering.

2 Materials and methods

2.1 Material preparation

The (001) rutile TiO_2 single crystal specimens (99.99%, MTI Corporation) were grown *via* the floating zone method, and subsequently EPI polished to have a surface roughness smaller than 5 Å. The single crystal substrate was sectioned into three pieces along the [100] direction. The rutile TiO_2 single crystal specimens used in this study are commercial single crystal substrates and their thickness is 0.5 mm. The sectioned specimens were subjected to heat treatment using an OTF-1200X furnace (MTI Corporation). A schematic illustration of the heat treatment history for the three specimens is shown in Fig. 1(a). All specimens were annealed at 600 °C for 300 min under atmosphere to remove potential preexisting oxygen vacancies from the product, and then the specimens were allowed to cool in the furnace. The specimen that was annealed only under atmosphere was labeled as pristine (PR) condition. The other two specimens were annealed at 700 °C for 60 min (R1) and 450 min (R2), respectively, with a constant flow of ultra-high purity 5% H_2 and 95% Ar gas mixture.

The transmittance spectra of the heat-treated specimens were collected using a Lambda 1050 with a 3D detector in the wavelength range of 240 to 1500 nm. X-ray diffraction (XRD) analyses were carried out using a PANalytical Empyrean X'pert PRO MRD diffractometer with a 2 × Ge (220) hybrid monochromator to select Cu $K\alpha_1$.

2.2 Mechanical property measurement

A Brucker TI premier nanoindenter equipped with a Berkovich indenter tip with an effective tip radius of 500 nm was employed to perform the indentation experiments along the [001] direction of the single crystal specimens under load-control mode. The maximum load (P_{max}) for each indent was 15 mN. A schematic of the indentation setup can be found in Fig. 1(b). 25 indents were performed on each specimen to ensure reproducibility. The fracture toughness was calculated based on the crack lengths measured from the SEM images of the indents. For each sample, 50 cracks were analyzed to ensure statistical reliability. The crack length was defined as the straight-line distance between the two tips of each radial crack emanating from the indent. The Oliver–Pharr method was employed to perform tip calibration on fused quartz before the indentations.[56]

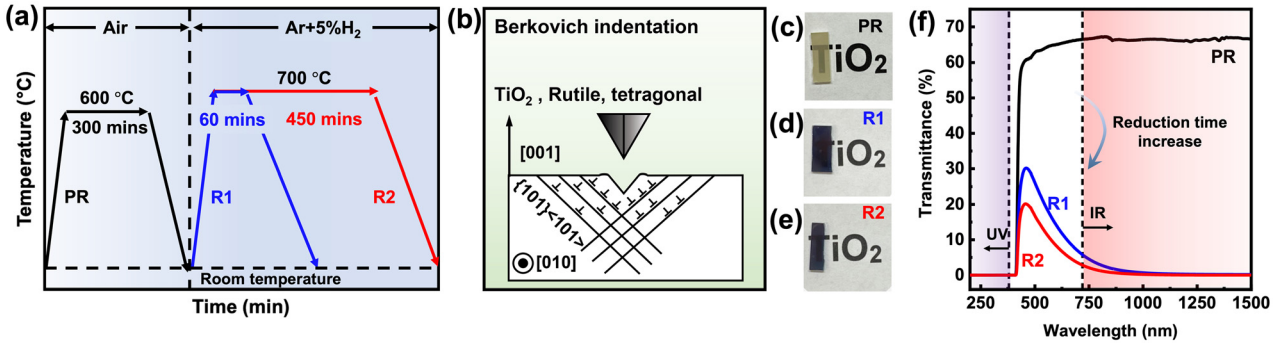

Fig. 1 (a) Schematic of the heat treatment history of each specimen. (b) Schematic of the nanoindentation experiment design. (c–e) Optical images of the pristine (PR) single crystal TiO_2, R1 (700 °C per 60 min) and R2 (700 °C per 450 min) specimens, respectively. (f) Transmittance profile of the specimens in the wavelength range of 240 to 1500 nm.

2.3. Microstructure characterization

Scanning electron microscopy (SEM) analysis was performed using a Thermo Fisher FEI Quanta 3D scanning electron microscope to examine the indents on each specimen. Furthermore, transmission electron microscopy (TEM) experiments were conducted to aid the understanding of the deformation behaviors of TiO_2. The preparation of the post-deformation TEM sample was performed using a Thermo Fisher Helios G4 Duo-beam SEM. Fig. S1 demonstrates a schematic illustration of the TEM sample lift-out region with respect to the indent. Bright-field (BF) and dark-field (DF) TEM experiments were conducted by using a Thermo Fisher Talos 200X TEM microscope operated at 200 kV, while high-resolution scanning TEM (HRSTEM) imaging was carried out using a Thermo Fisher Themis-Z operated at 300 kV equipped with a spherical aberration corrector. Crystal misorientation angles were collected with an automated crystal orientation mapping system, ASTAR, a precession electron diffraction-based technique developed by NanoMEGAS.

3 Results

3.1 Sub-stoichiometric TiO_2 produced by hydrogen reduction

Fig. 1c–e display the optical images of the PR, R1, and R2 specimens, respectively. An obvious color change (blackening) can be seen in the hydrogen-reduced R1 and R2 specimens. Fig. 1f shows the transmittance spectra of the three specimens in the wavelength range of 250 to 1500 nm. The transmittance spectrum of PR exhibits an average transmittance of 65% over the range of 380 to 1500 nm (visible and near infrared range). After hydrogen reduction, both the R1 and R2 specimens exhibited a sharp decrease in transmittance in the visible wavelength range. The R2 specimen shows a peak transmittance of 20% compared to that of ~30% for the R1 specimen in the same wavelength range. The transmittance of both R1 and R2 diminished significantly in the near infrared wavelength range.

The inverse fast Fourier transform of the high-resolution TEM (HRTEM) micrographs and corresponding FFTs of the undeformed PR, R1, and R2 specimens in Fig. 2a–c were used to measure the interplanar spacing of their {200} planes (d_{200}) and {002} planes (d_{002}). The calculated lattice parameters for each specimen are shown in Fig. 2d. After reduction in hydrogen for 60 min (R1), both lattice parameters along the *a* and *c* axes expanded. The specimen that underwent longer reduction treatment (R2) shows evident lattice contraction. In the undeformed lattice of PR (Fig. 2a) and R1 (Fig. 2b), no obvious defect can be detected. The XRD patterns shown in Fig. 2(e) reveal that the (002) diffraction peaks of the PR, R1, and R2 samples appear at different positions. Using the Bragg equation, the corresponding lattice constants (*c*-values) were calculated and presented in Fig. 2(f). As the reduction time increases, the lattice constant c first increases, and then decreases, exhibiting a trend that is consistent with the inverse FFT-based lattice measurements shown in Fig. 2(d).

3.2 Mechanical properties of TiO_2 prepared under different reduction conditions

To introduce dislocations in the samples, we used a relatively small load of 15 mN at a small indentation depth of 150 nm. The load and depth were selected to ensure that the indentation marks were visible in the following SEM and TEM study of the indented areas. 25 indents at the peak load of 15 mN were performed on each specimen. Fig. 3a shows the load-depth (*P*–*h*) curves for the three specimens. In Fig. 3(a), only one representative *P*–*h* curve is shown for each condition. The hardness values presented in Fig. 3(b) are the average values calculated from 25 measurements. Fig. 3b and c summarize the average hardness and average first pop-in loads (P_{crit}) for the specimens, respectively. The lightly reduced R1 exhibits an obvious increase in hardness compared to the stoichiometric PR. The heavily reduced R2 does not show a significant increase in hardness compared to the R1 condition, although it was reduced for a much longer time. Fig. 3c shows that hydrogen reduction can effectively reduce P_{crit}. The 60 min reduction treatment was able to reduce the P_{crit} from 5.05 ± 0.6 mN for the stoichiometric PR to 2.55 ± 0.8 mN for the slightly reduced R1. The P_{crit} increased slightly to 3.48 ± 0.5 mN for the heavily reduced R2 specimen.

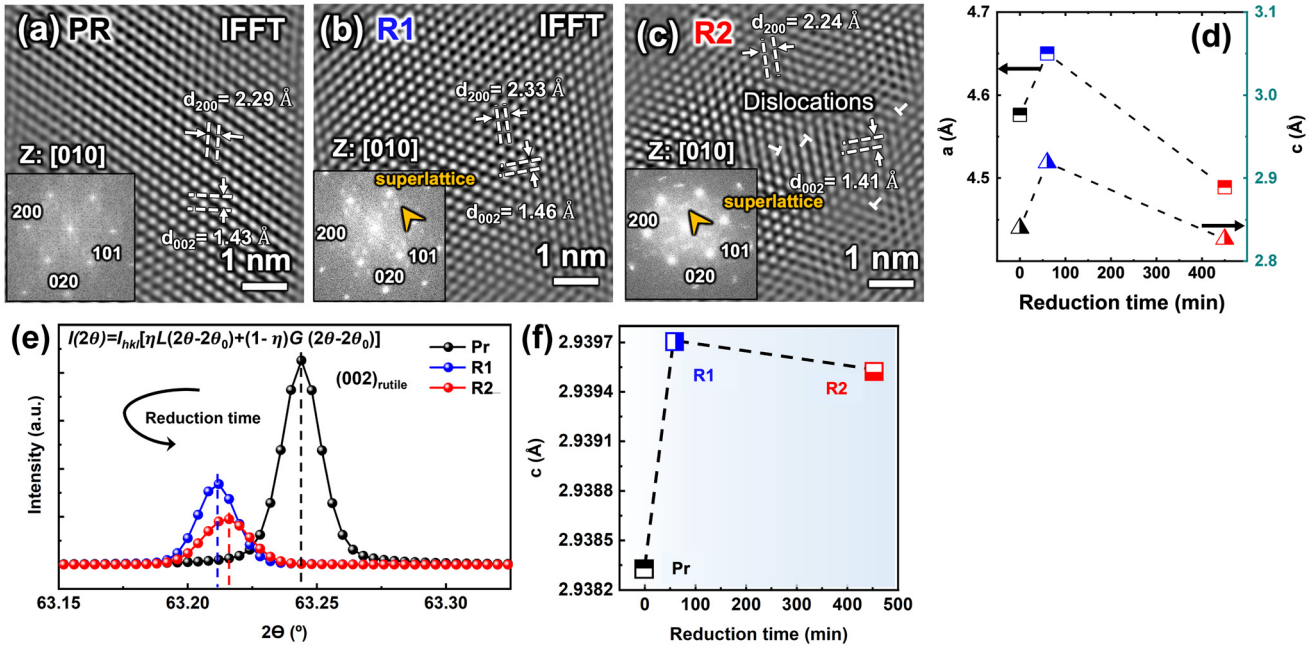

Fig. 2 (a–c) Inverse fast Fourier transform (IFFT) micrographs of undeformed PR, R1 and R2 specimens along the [010] zone axis with the inserted fast Fourier transform pattern. (d) Measured average lattice spacing along the *a* and *c* axis for each specimen. Squares represent lattice parameter *a*, corresponding to the left *Y*-axis, while triangles represent lattice parameter *c*, corresponding to the right *Y*-axis. (e) X-ray diffraction patterns for each specimen fitting using the Pseudo-Voigt model. (f) Calculated lattice spacing along the *c* axis for different oxygen compositions.

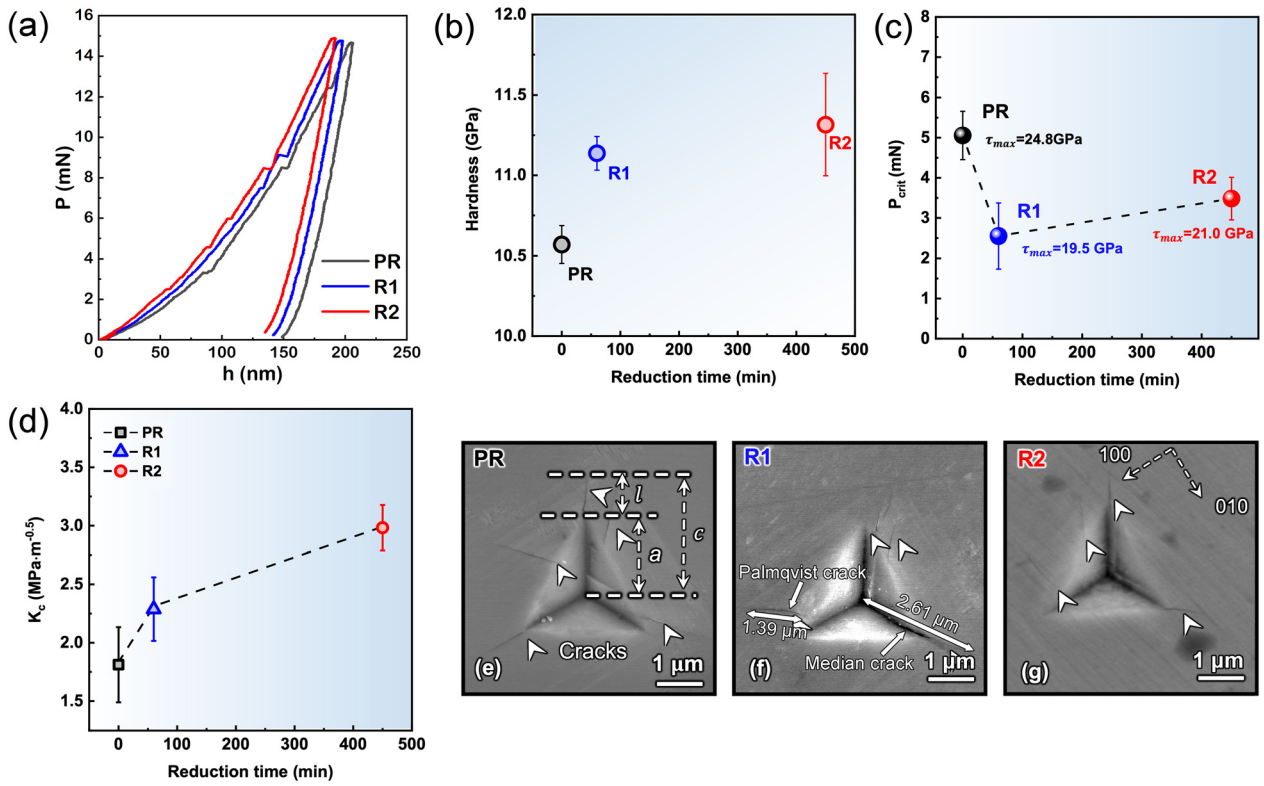

Fig. 3 (a) *P*–*h* curves for PR (black), R1 (blue), and R2 (red) specimens deformed to a P_{max} of 15 mN. (b) Plot of the average hardness at different oxygen concentrations. (c) Average first $P_{pop\text{-}in}$ as a function of reduction time. (d) Average fracture toughness at different reduction times. (e–g) SEM micrographs of the indents in the specimens loaded to the P_{max} of 15 mN with arrows pointing to the deformation-induced cracks.

The fracture toughness (K_c) for each specimen was calculated using the following equation:

$$K_c = 0.016\left(\frac{a}{c}\right)^{0.5}\left(\frac{E}{H}\right)^{\frac{2}{3}}\frac{P}{c^{\frac{3}{2}}}, \quad (2)$$

where a is the length of the vertex of the indent, l is the length of the vertex crack, c is the length from the center point of the indent to the tip of the vertex crack ($c = a + l$), E is the Young's modulus of the sample, H is the hardness value, and P is the max applied load (P_{max} = 15 mN). The Young's modulus and the hardness values used for calculating K_c for each specimen are summarized in Table S1. As shown in Fig. 3d, after the 60 min reduction treatment, the K_c of the single-crystal TiO_2 increased from 1.81 ± 0.3 MPa $m^{1/2}$ to ~2.3 ± 0.2 MPa $m^{1/2}$. Albeit having a similar hardness to R1, the R2 specimen exhibited a further enhancement in fracture toughness (3.0 ± 0.2 MPa $m^{1/2}$) compared to R1. Fig. 3e–g show the SEM micrographs identifying the cracks and measurements of a, c, and l for the PR, R1 and R2 specimens, respectively.

3.3 Post-mortem deformation behavior analyses

To investigate the origin of the increase in hardness and fracture toughness, detailed post-mortem TEM analyses were carried out to investigate the deformation behavior of the specimen with hydrogen reduction. Fig. 4a shows a cross-sectional bright-field (BF) TEM micrograph of an indent on the PR specimen. Immediately underneath the indent, stacking faults (SF) with {101} and {10$\bar{1}$} habit planes can be observed. The two sets of SFs intersect with each other as they propagate downward. Dislocations that are trailing down from the SF can be identified at the lower portion of the TEM specimen. The propagation direction of dislocations is observed to be [002]. Fig. 4b shows the two-beam-dark-field (TBDF) TEM micrograph with $\vec{g} = [002]$ in the same region, which reveals the dislocations in bright contrast (labeled by white arrows). Thorough $\vec{g} \cdot \vec{b}$ analysis revealed that the dislocations with bright contrast in Fig. 4b mostly have the common $\vec{b} = [001]$ (an example of the full $\vec{g} \cdot \vec{b}$ analysis can be seen in Fig. S3 and Table S2). The vertical dislocation lines with the line vector of the [001] direction are screw dislocations with $\vec{b} = [001]$, while the horizontal dislocation lines with the line vector of the [100] direction are edge dislocations with $\vec{b} = [001]$. The other curved dislocations are classified as mixed dislocations with $\vec{b} = [001]$. Fig. 4c is an inverse pole figure (IPF) of the region in Fig. 4a. The IPF reveals that the region under the indent mostly has the same out-of-plane orientation. Fig. 4d demonstrates the point-to-origin misorientation profile along line d in Fig. 4c. According to Fig. 4d, most of the points crossing the line have misorientation angles less than 10° with a few exceptions showing point-to-origin misorientation angles reaching ~40°. However, since there were no obvious crystallographic defects detectable at those points, these spotty high misorientation angle data can be attributed to the formation of dislocations and stacking faults after indentation.

Fig. 5a shows the cross-sectional BF TEM micrograph of the indent on the R1 specimen. Similar to PR, intersecting SFs with {101} and {10$\bar{1}$} habit planes can be observed. In addition, thick shear bands (SBs) along {$\bar{1}$1$\bar{1}$} can be identified. These SBs appear as distinct bands within the deformed region. Notably, these features were not present in the PR or R2 samples. The HRTEM image in Fig. 5b reveals the presence of (101) and (10$\bar{1}$) SFs. The corresponding FFT pattern shown in the inset further confirms this finding, as evidenced by the presence of two sets of intersecting streaks. Fig. 5c shows the weak-beam DF micrograph of a similar region in Fig. 5a with $\vec{g} = [002]$. Edge, screw, and mixed dislocations with $\vec{b} = [001]$ trailing down from the planar faults are evident in Fig. 5d. Interestingly, in the region above the SBs, most dislocations are (vertical) screw dislocations, whereas below the SBs, (horizontal) edge dislocations appear to be the dominant dislocations. The IPF (Fig. 5d) clearly demonstrates a lattice transformation region (purple color) underneath the indent. The point-to-origin misorientation profile (Fig. 5e) of line d in Fig. 5d reveals that the transformed region has a consistent 90° misorientation angle with the matrix. Fig. 6a shows a high-

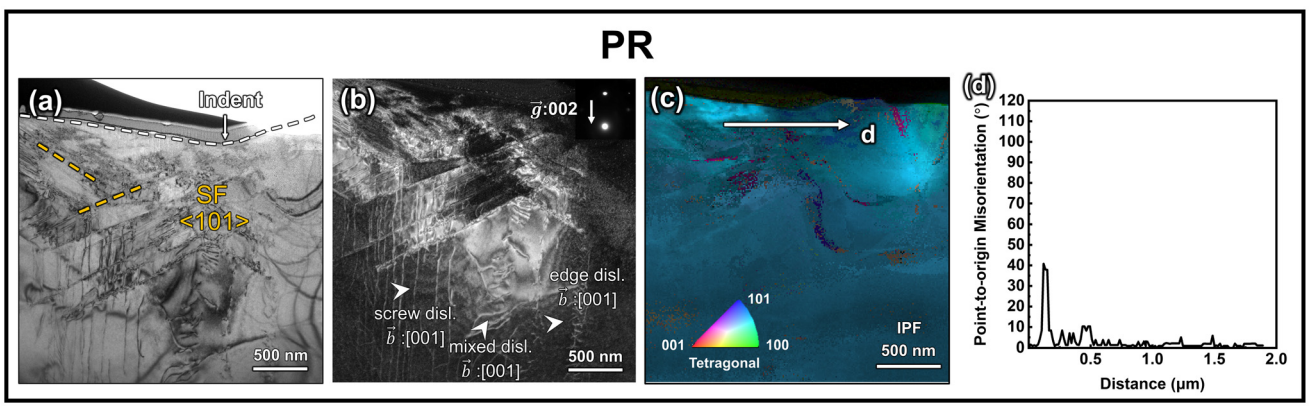

Fig. 4 (a) Bright-field (BF) TEM micrograph showing the cross-sectional view of the indent on the PR specimen deformed at a P_{max} of 15 mN. (b) Dark-field (DF) TEM micrograph of the region in (a) under two-beam condition with the $\vec{g} = [002]$. (c) Inverse pole figure (IPF) of the same region in (a). (d) Point-to-origin misorientation plot along line d in (c).

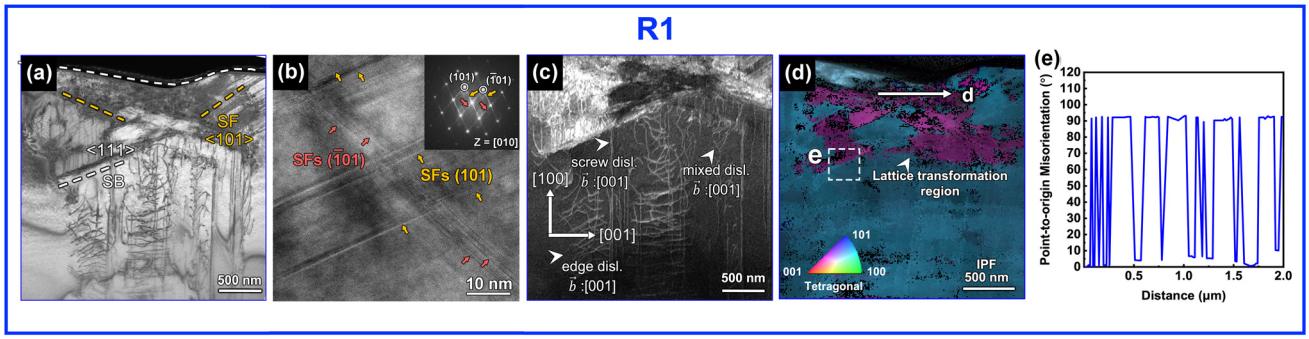

Fig. 5 (a) BF TEM micrograph showing the cross-sectional view of the indent on the R1 specimen deformed to a P_{max} of 15 mN. (b) High-resolution TEM (HRTEM) image showing the (101) and (1̄01) stacking faults, marked by arrows, respectively. Inset: corresponding FFT pattern with two sets of diffraction streaks confirming the presence of stacking faults. (c) WBDF TEM micrograph of the region in (a) with $\vec{g} = [002]$. (d) IPF map of the region in (a). (e) Point-to-origin misorientation plot of line d in (d).

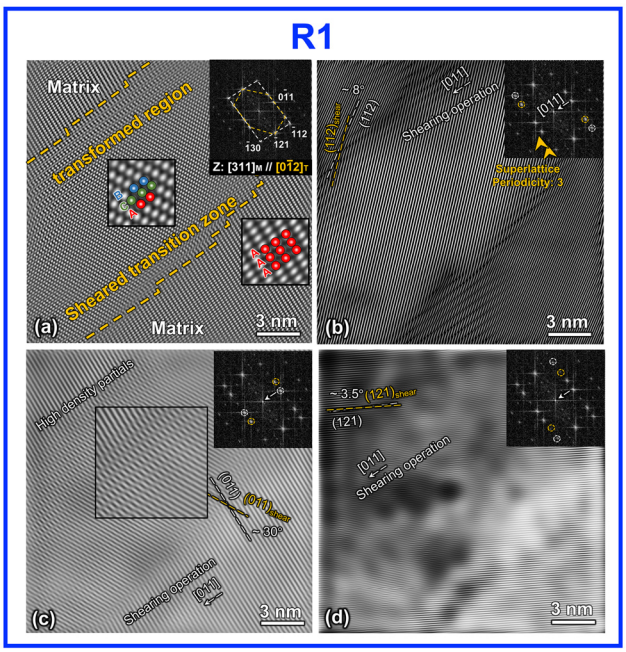

Fig. 6 (a) High-resolution scanning transmission electron microscopy (HRSTEM) micrograph of the R1 specimen in region e in Fig. 5(d), with insets showing the atomic arrangement in the transformed region and the matrix region. (b) Selected filtered IFFT micrograph showing the (112) planes and $(112)_{shear}$ planes. (c) Selected filtered IFFT micrograph showing the (011) planes and $(011)_{shear}$ planes. (d) Selected filtered IFFT micrograph showing the (121) planes and $(121)_{shear}$ planes.

resolution STEM (HRSTEM) micrograph of box e in Fig. 5d, showing the atomic arrangement transformation from the matrix to the transformed region. The Ti stacking sequence in the undeformed matrix along the [311] zone axis is AAA, while the Ti stacking sequence in the transformed zone shifted to ACB. Super lattice spots with a periodicity of three that are parallel to the [1̄21] diffraction spots can be observed in the inserted FFT pattern (Fig. 6a). The crystallography analyses revealed that after deformation, a stress-induced crystal rotation took place. The transformed region was identified as rutile TiO_2 with a zone axis of $[0\bar{1}2]_T$, which is parallel to the $[311]_M$ zone axis of the surrounding matrix. The detailed inverse FFT analyses by selecting a pair of matrix spots and the corresponding sheared spots are shown in Fig. 6b and c, respectively. In Fig. 6b, the selected matrix spot corresponds to the (112) planes and the corresponding sheared planes are denoted as $(112)_{shear}$. The sheared transition zone in Fig. 6b shows an obvious (112) lattice plane shearing operation with the $\frac{1}{2}[011]$ vector in every three atomic layers, which corresponds well with the superlattice with periodicity of three. The rutile (112) planes gradually deviated from their original orientation as they went through the successive shear operations. The $(112)_{shear}$ planes have an 8° deviation compared to the original rutile (112) planes after the shearing deformation. Fig. 6c shows the inverse FFT image of the (011) planes and $(011)_{shear}$ planes. The lattice gradually rotated to have a 30° deviation from the original (011) planes through the shear operations of the (011) planes along the $\frac{1}{2}[011]$. Similar shear operations along $\frac{1}{2}[011]$ in Fig. 6b and c can also be identified for the (121) planes, as shown in Fig. 6d. The deviation of the $(121)_{shear}$ from the original (121) planes is 3.5°. Furthermore, interstitial loops can also be observed. The evolution from the matrix to the transformed region can be attributed to the result of a series of shear operations of (112), (011) and (121) planes along the $\frac{1}{2}[011]$ vector.

The cross-sectional BF TEM micrograph of the indent for the R2 specimen is shown in Fig. 7a. SFs with {101} and {10$\bar{1}$} habit planes SFs can be found in the region underneath the indent. Fig. 7b shows the TBDF of the same region in Fig. 6a with $\vec{g} = [002]$. In the deformed R2 specimen, vertical screw dislocations with $\vec{b} = [001]$ are dominant, while few horizontal edge dislocations can be seen. The IPF (Fig. 6c) shows that the lattice transformation in the deformed R2 crystal is highly localized and has various configurations compared with the continuous and single transformation configuration in the R1 specimen. The point-to-origin misorientation profile of line d (in Fig. 7c) shown in Fig. 7d confirmed that in contrast to the primarily 90° misorientation shown in the R1 condition, the

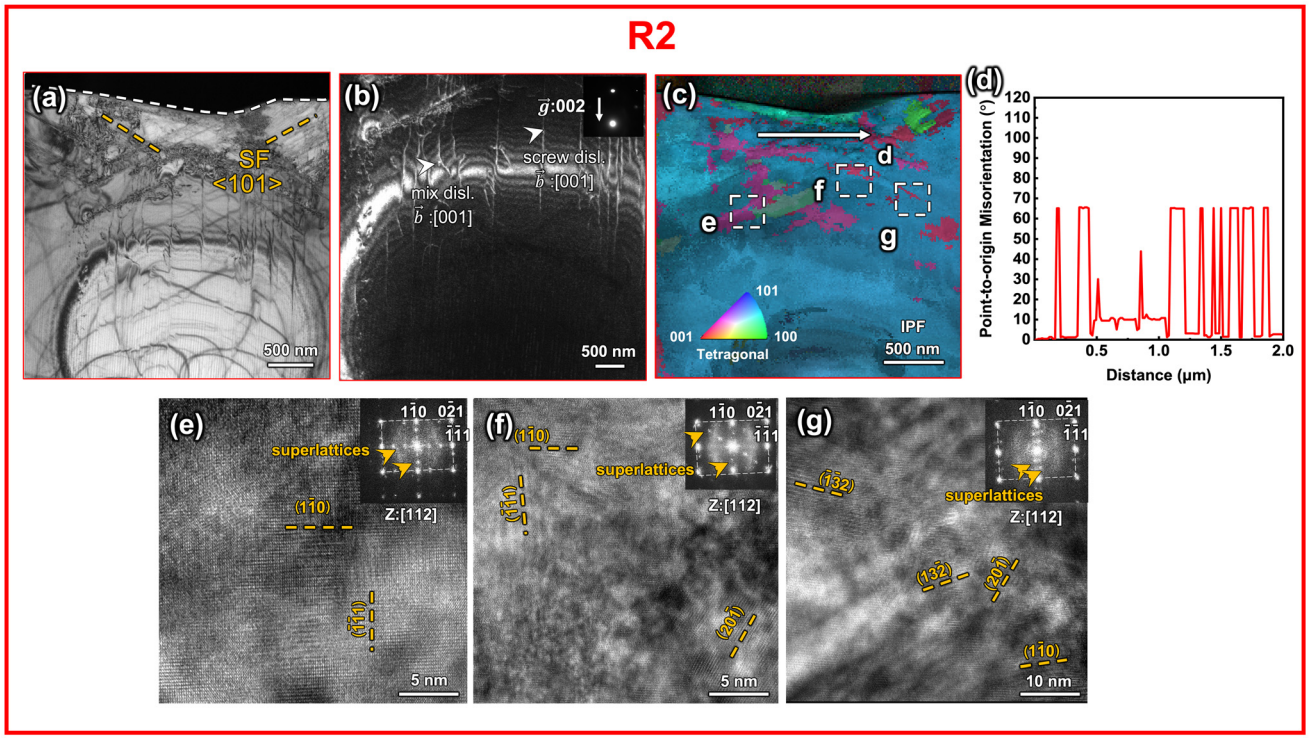

Fig. 7 (a) BF TEM micrograph showing the cross-sectional view of the indent on the R2 specimen deformed at a P_{max} of 15 mN. (b) WBDF TEM micrograph of the region in (a) with $\vec{g} = [002]$. (c) IPF of the same region. (d) Point-to-origin misorientation plot along line d in (c). (e–g) HRTEM micrographs showing various sub-stoichiometric phases in the corresponding region shown in (c).

lattice transformation has multiple configurations, including 65°, 30°, 45°, and 10°. Fig. 7e–g show HRTEM micrographs of the boxed regions e, f, and g in Fig. 7c, respectively, showing the atomistic arrangements of the deformed regions. The transformed regions consist of highly ordered CSPs with the habit planes of (1$\bar{1}$0), (1$\bar{1}$1), (20$\bar{1}$), (1$\bar{3}$2), and (13$\bar{2}$).

TBDF TEM analyses revealed that the dislocation density and configuration can vary drastically depending on the oxygen reduction extent. The line interception method and convergent beam thickness determination method were used to estimate the dislocation density in each deformed specimen.[57,58] The dislocation density (ρ_l) was estimated using the following equation:[58]

$$\rho_l = \frac{2n}{Rt} \quad (3)$$

where n is the number of dislocation interceptions along the line, R is the length of the line (2 μm), and t is the thickness of the TEM specimen foil. The thickness measurement for each TEM specimen is shown in Fig. S4. The estimated dislocation densities for the deformed PR, R1, and R2 crystals are 4.3 × 10^{13} m^{-2}, 7.5 × 10^{13} m^{-2}, and 6.3 × 10^{13} m^{-2}, respectively (Fig. 8a). The deformed R1 specimen has the highest dislocation density, which is a ~78% higher compared to the deformed PR case. The further reduced R2 specimen shows a slightly lower dislocation density compared to the R1 case. In Fig. 4b, 5c, and 7b, dislocations can be observed under the TBDF imaging conditions with the diffraction vector $g = [002]$. Under these conditions, only dislocations with Burgers vector $b = [001]$ are visible. In the images, the vertical direction corresponds to [001], while the horizontal direction corresponds to [100]. This orientation arises from the sample preparation process, in which the FIB lift-out was performed on single-crystal TiO_2 by sectioning parallel to the [100] direction, with the cutting direction oriented along [001].

Therefore, the dislocations aligned along the vertical [001] direction are parallel to $b = [001]$, indicating that they are screw dislocations. The dislocations aligned along the horizontal [100] direction are perpendicular to $b = [001]$, corresponding to edge dislocations. The dislocations oriented in other directions are considered mixed-type. Based on these geometric relationships, the densities of screw and mixed dislocations were separately quantified. Fig. 8b illustrates the distribution of the different dislocation types, screw, edge, and mixed, in each specimen after deformation, and serves to demonstrate how the variation in oxygen vacancy concentration affects not only the total dislocation density but also the types of dislocations. The observed shift in dominant dislocation type from screw dislocations in the pristine (PR) specimen to edge dislocations in the lightly reduced R1 specimen, and back to screw dislocations in the heavily reduced R2 specimen indicates a clear correlation between the defect chemistry and deformation mechanism. This variation is critical to understand how oxygen vacancies influence the slip behavior, dislocation mobility, and ultimately the plasticity and toughening mechanisms in reduced TiO_2. Thus, Fig. 8b is significant in

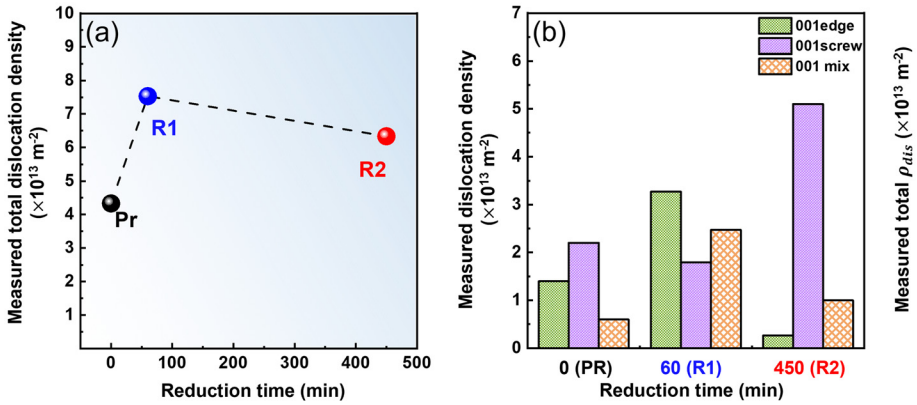

Fig. 8 (a) Measured total dislocation density *vs.* reduction time. (b) Comparison of the density of different types of dislocations for each specimen.

revealing the underlying defect-mediated deformation pathways in response to different levels of oxygen deficiency. In the deformed PR specimen, screw dislocation with $\vec{b} = [001]$ is the preferential dislocation configuration, while in the deformed R1 specimen, edge dislocation with $\vec{b} = [001]$ is the most popular dislocation configuration. In the deformed R2 specimen, the population of the edge dislocation and mixed dislocation with $\vec{b} = [001]$ sharply reduced, while ~80% of the dislocations in the deformed R2 specimen are screw dislocations with $\vec{b} = [001]$.

4 Discussion

4.1 Microstructure evolution: lattice expansion and contraction

In this study, O vacancies, $V_O^{\cdot\cdot}$, were introduced into rutile TiO_2 single crystals by hydrogen reduction. The major difference between the R1 and R2 specimens is the hydrogen reduction time. The longer reduction time (450 min) for R2 is expected to introduce a larger number of oxygen vacancies into the specimen compared to the 60 min reduction time for R1. The monotonic reduction in optical transmittance from PR to R1 and R2 confirmed that an increase in the reduction time leads to a higher defect population in the annealed crystals.[39,41,42] The HRTEM and XRD analyses both demonstrate that initial hydrogen reduction (R1) led to TiO_{2-x} lattice expansion, while a longer reduction time (R2) resulted in lattice contraction. This trend is in good agreement with the literature.[42,48] The FFT pattern shown in Fig. 2b demonstrates superlattice spots with a periodicity of 3 along the [101] and [10$\bar{1}$] directions as a result of the highly ordered $V_O^{\cdot\cdot}$ at the corresponding crystal planes.[18,54,59,60] The FFT pattern for the undeformed R2 specimen shown in Fig. 2c reveals that in the more reduced R2, the superlattice spots along the [101] and [10$\bar{1}$] directions do not appear as discrete spots but emerge as thin streaks, indicating that the $V_O^{\cdot\cdot}$ are less ordered in the R2 specimen. Additional superlattice spots along [002] and [20$\bar{1}$] can also be observed in R2 due to the formation of new ordered $V_O^{\cdot\cdot}$ along those planes after further reduction. No evidence of the formation of Magnéli phases was observed in these three samples, as none of the SAED patterns or FFT images obtained from various regions exhibited the characteristic satellite spots or streaks along the [001] direction that typically arise from periodic shear planes or planar defects.[50,59,60] This suggests that the examined specimens did not contain obvious Magnéli-type structures. The initial lattice expansion induced by the reduction reaction can be attributed to the larger radius of Ti^{3+} ions, which were reduced from the smaller Ti^{4+} ions, the weakened Ti–O bonding strength, and the increase in average Ti–O bond length.[48] Therefore, the value of x in TiO_{2-x} for the R1 specimens is less than 0.0015, which is the solubility limit of $V_O^{\cdot\cdot}$ in rutile TiO_2.[51] The lattice contraction in the R2 specimen induced by further reduction can be a result of the coalescence of $V_O^{\cdot\cdot}$, leading to lattice collapse and shear plane formation as the $V_O^{\cdot\cdot}$ concentration exceeds the matrix solubility.[48,54] The presence of dislocations in the as-reduced R2 specimen can be an indication of the occurrence of shear events. Hence, the x value for TiO_{2-x} in the R2 specimen is ≥0.015, and thus there are more oxygen vacancies available in the R2 specimen than in the R1 specimen.

4.2 Deformation behavior in stoichiometric TiO_2

In the case of the rutile TiO_2 single crystal with the indentation direction parallel to [001], its primary slip systems are [101] ($\bar{1}$01) and [$\bar{1}$01] (101). To investigate whether the first pop-in event corresponds to the activation of the slip systems and dislocation nucleation, the theoretical shear strength of the crystal (τ_{th}) and the maximum shear strength for the indentation (τ_{max}) were calculated. The theoretical shear strength refers to the stress required to activate the primary slip systems in a defect-free crystal using eqn (1). The measured E for the PR specimen is 326 GPa. Thus, the τ_{th} for PR is ~20.4 GPa. Alternatively, τ_{max} refers to the stress to initiate the first pop-in event, which can be calculated as follows:[55]

$$\tau_{max} = 0.31\left(\frac{6E_r^{\,2}}{\pi^3 R^2}P_{crit}\right)^{\frac{1}{3}} \quad (4)$$

The calculated τ_{max} for PR is 24.8 GPa, which is on par with the estimated τ_{th}. Therefore, the first pop-in event observed in

the *P–h* curve can be correlated to the activation of the primary slip system. Prior studies have used a similar approach to probe the nucleation of dislocations from pop-in events observed in nanoindentation experiments.[61–63] SFs with habit planes of (101) and ($\bar{1}$01) can be observed in the deformed PR specimen. The formation of these SFs can be attributed to the dissociation of the dislocations generated by the activation of the [101] ($\bar{1}$01) and [$\bar{1}$01] (101) slip systems. The reactions for full dislocations to dissociate into partial dislocations are as follows:

$$[101] \rightarrow \frac{1}{2}[101] + \frac{1}{2}[101] \quad (5)$$

$$[\bar{1}01] \rightarrow \frac{1}{2}[\bar{1}01] + \frac{1}{2}[\bar{1}01] \quad (6)$$

The dissociation is energetically favorable as the reaction can reduce the overall line energy.[31,53] As shown in Fig. 4b, the SFs produced by the aforementioned reactions can intersect and further react to form dislocations with a Burgers vector of ⟨001⟩, as described in the following equation:[31]

$$\frac{1}{2}[\bar{1}01] + \frac{1}{2}[101] \rightarrow [001] \quad (7)$$

In the deformed PR specimen, the screw dislocation with a Burgers vector of ⟨001⟩ is the more popular dislocation configuration compared to the edge dislocation with the same Burgers vector. This phenomenon can be attributed to the lower dislocation energy for the screw ⟨001⟩ dislocation compared to its edge counterpart.[53] The deformation behaviors of the PR stoichiometric TiO_2 specimen discussed in this section serve as the baseline to understand the effect of oxygen vacancies on the deformation behavior in sub-stoichiometric TiO_{2-x}.

4.3 Deformation behavior in sub-stoichiometric TiO_{2-x}

As discussed in the result section, the major differences between the deformation behavior in the reduced R1 and R2 specimens compared to the stochiometric PR specimen are (1) hardness, (2) first pop-in stress, (3) lattice distortion, and (4) dominant dislocation configuration and density. As shown in Fig. 3(c), both R1 and R2 possess higher hardness compared to the stoichiometric PR specimen. The same observation has been reported by Dellacorte *et al.* In their report, the hardness of the single crystalline TiO_{2-x} specimen increases monotonically as x increases until x is greater than 0.15.[30] In this case, as both the R1 and R2 specimens have x smaller than 0.015, the higher the extent of reduction, the greater the hardness. Therefore, the heavily reduced R2 has the highest hardness among the three specimens. DellaCorte *et al.* theorized that the increasing hardness in reduced TiO_{2-x} can arise from the activation of its low shear strength slip planes through the solid lubrication effect from the creation of oxygen vacancies.[30] However, due to technology limitation, they were not able to estimate the τ_{CRSS} for the specimens. In this work, the τ_{CRSS} for R1 and R2 were calculated to be 19.5 GPa and 21.0 GPa, respectively. Both reduced specimens exhibit noticeably lower τ_{CRSS} compared to the PR specimen (24.8 GPa). This observation validated the hypothesis that the τ_{CRSS} of the rutile crystal can be reduced by introducing a small amount of oxygen vacancies. A similar trend has recently been reported by Stich *et al.* for H_2-reduced single-crystal $SrTiO_3$, confirming that this trend can be applicable to other ceramic materials as well.[33] The reduction in τ_{CRSS} can be a result of the weakened Ti–O bonds due to the introduction of oxygen vacancies.[48] Ashbee *et al.* ascribed the origin of the oxygen deficiency-induced hardening effect to the work hardening from the activation of the extra {110}[001] slip system due to the reduced τ_{CRSS} and the aggregation of point defects along dislocations.[30–32] In our study, the detailed TEM analyses revealed that dislocations with $\vec{g} = [001]$ can be observed in all three specimens. However, the dislocation density with $\vec{g} = [001]$ in the R1 and R2 specimens is much higher than that in the PR specimen, and thus provides more work hardening. The formation of dislocations with $\vec{g} = [001]$ can be a result of the reaction of the partial dislocations $\frac{1}{2}$[101] and $\frac{1}{2}$[$\bar{1}$01], which are dissociated from dislocations from the primary slip system.[31] In addition, Li *et al.* reported that oxygen vacancy can effectively reduce the stacking fault energy in TiO_2, which can facilitate full dislocation dissociation.[11] In summary, oxygen vacancies can reduce the τ_{CRSS} and stacking fault energy, allowing easy slip along the primary slip system, and facilitate the dissociation of full dislocations into partial dislocations. The increase in these partial dislocations and their interactions lead to the elevation of the [001] dislocations. The [001] dislocations can further react with the ⟨101⟩ dislocations, leading to work hardening in reduced TiO_2.[31] As deformation progressed, these two types of dislocations were frequently found to intersect or interact within the shear transition zones. These interactions can result in the formation of dislocation junctions, entanglements, or barriers that hinder further dislocation motion. This accumulation and interaction of dislocations contribute to strain hardening by increasing the resistance to plastic deformation. Therefore, the observed hardening behavior can be attributed to the interactions between the primary ⟨101⟩ dislocations and the [001] dislocations. Interestingly, in the PR TiO_2, edge, screw and mixed dislocations with $\vec{g} = [001]$ coexist. The screw dislocation has the highest population in the PR TiO_2. In the R1 specimen, all three dislocation configurations are detected, and the dominant dislocation configuration is the edge dislocation. In the R2 specimen, the population of edge dislocations is low, while the screw dislocation becomes the dominant configuration. Motohashi *et al.* reported that in rutile TiO_2, edge dislocation for the {110}[001] slip system has a higher energy factor compared to mixed dislocations and screw dislocations, making the edge dislocations energetically unfavorable.[53]

In both R1 and R2, crystal rotation can be observed. In the R1 specimen, the {121} and {110} lattice planes sheared along the $\frac{1}{2}$[011] direction. The formation of shear bands exclusively in the R1 sample is likely related to the specific defect structure induced by the intermediate reduction in Fig. 5(a). At this reduction level, the concentration of oxygen vacancies may be

optimal for activating localized shear deformation along crystallographically favorable planes. In contrast, the PR sample lacks sufficient lattice defects to facilitate shear band formation. The alignment of the SBs with the $\{\bar{1}11\}$ planes suggests that these features are not random but are governed by the crystallographic slip mechanisms inherent to the rutile structure. The shear operations lead to local crystal lattice rotation (Fig. 6). In R2, CSP formation along multiple planes, $\{13\bar{2}\}$, $\{1\bar{1}0\}$, $\{\bar{1}11\}$ and $\{20\bar{1}\}$, can be observed in Fig. 7e–g. The superlattices with a periodicity of 3 indicate the transformation from a rutile TiO_{2-x} structure to Ti_3O_5.[52,64] These shear operations have been extensively reported in the formation of a Magnéli phase due to the local coalescence of oxygen vacancies.[36,45,50–52,54,64] The higher number of planes available for shear operation in the more reduced R2 is correlated to the superlattices induced by ordering of the oxygen vacancies in these planes before deformation. It is worth noting that in the undeformed R1 specimen, the oxygen vacancy concentration is low due to its short reduction time. No CSP formation took place before deformation. The lattice distortion and phase transformation observed in the post-deformation specimens in R1 indicate that an external drive may drive the diffusion of oxygen vacancies from the vicinity of the strained region to increase the local oxygen deficiency. The increase in local oxygen deficiencies facilitates the formation of CSP due to the coalescence of the excessive oxygen vacancies.[36,51] Li *et al.* observed the formation of a metastable substoichiometric CuO_{1-x} phase due to the diffusion of oxygen vacancies driven by external stress at room temperature. They reported that oxygen vacancies diffuse from the regions under tension to the regions under compression.[65,66] The prevalence of edge dislocation with $\vec{b} = [001]$ in R1 can also be related to the formation of a continuously transformed region (purple region in Fig. 5d). As shown in Fig. 5a, the horizontal edge dislocations mostly exist under the $(0\bar{1}1)$ CSPs, at the end of the transformed region. This observation indicates that the edge dislocations were emitted from the interface between CSPs and the matrix. The exact mechanism for the formation of the [001] screw dislocations is still unclear. To further understand this phenomenon, detailed calculation and atomistic simulation can be beneficial in the future.

Finally, as shown in Fig. 3d, an increase in the fracture toughness for the reduced R1 and R2 specimens compared to the pristine PR specimen can be observed. Despite their comparable hardness and dislocation density, the R2 specimen shows a higher fracture toughness than the R1 specimen. The increasing toughness for both reduced specimens (than the PR TiO_2) can be attributed to their higher dislocation density and the shear operation induced by the annihilation of oxygen vacancies. Porz *et al.* reported that high density pre-existing dislocations can effectively toughen single-crystal $SrTiO_3$. They attributed the toughening to the room temperature dislocation mobility in $SrTiO_3$. The pre-existing dislocations can carry plasticity at low stress (~60 MPa) without the necessity to reach extremely high stress (17 GPa) to nucleate dislocations.[4,12,13] TiO_2 is believed to have no room temperature dislocation mobility.[2] However, Moon *et al.* reported the observation of dislocation toughening in Al_2O_3, which is also believed to have no dislocation mobility at room temperature.[2,15] Therefore, the increase in dislocation density induced by the reduced τ_{CRSS} and stacking faults can be one of the contributing factors to the toughening mechanism in oxygen-deficient TiO_2. In addition, deformation can be accommodated by a phase transformation induced by oxygen vacancy coalescence in oxygen-deficient TiO_2. Furthermore, the Magnéli phases formed by the coalescence of oxygen vacancies can further toughen the crystal.[30,45,67] The higher concentration of oxygen vacancies and the Ti_3O_5 phase transformation may contribute to the higher fracture toughness in R2 than the R1 specimen.

5. Conclusion

The deformation behaviors of oxygen-deficient rutile TiO_{2-x} single crystals modified by hydrogen reduction were investigated in detail in this study. Nanoindentation experiments revealed that oxygen deficiency is effective to reduce τ_{CRSS}, leading to easier slip occurrence and activation of the secondary $\{110\}[001]$ slip systems. The interactions between the primary $\langle 101\rangle$ dislocations and the [001] dislocations lead to hardening in the oxygen-deficient TiO_{2-x} specimens through work hardening. Post-deformation analyses demonstrated that oxygen vacancies can be aligned by external stress, resulting in local oxygen vacancy coalescence and shear plane formation. In the slightly reduced R1 specimen, deformation is assisted by crystal rotation enabled by successive shear of the $\{121\}$ planes. In the heavily reduced R2 specimen, a phase transformation from rutile TiO_2 to Ti_3O_5 took place along several shear planes. Oxygen vacancies can toughen TiO_2 by reducing the dislocation nucleation barrier, activation of additional slip systems, increasing the dislocation density, grain fragmentation and rotation, and local phase transformation through the coalescence of oxygen vacancies. These findings provide general guidelines and approaches for the future designs of room temperature ductile ceramics.

Author contributions

BY and ZH performed sintering experiments, and BY prepared the first draft of the manuscript. NR and ZS worked with BY on TEM and HRTEM experiments. HD and JS performed optical measurements. REG, NB and CSH helped with vacancy and dislocation analysis. HW and XZ helped to design the experiments and analyze results. HL helped to analyze TEM images and prepare the response to reviewers and worked on the revised manuscript. All authors were involved in discussion on the manuscript and revised the manuscript.

Conflicts of interest

There are no conflicts to declare.

Data availability

The data supporting this article have been included as part of the SI.

SI: Table S1 and S2, Fig. S1–S3. See DOI: https://doi.org/10.1039/d5nr02684a.

Acknowledgements

This work was supported by the U.S. Office of Naval Research N00014-22-1-2160. We would also like to acknowledge the access to the Purdue electron microscopy facility.

References

1 G. Schoeck, Dislocation Theory of Plasticity of Metals, *Adv. Appl. Mech.*, 1956, **4**, 229–279, DOI: 10.1016/S0065-2156(08)70374-0.

2 L. Porz, 60 years of dislocations in ceramics: A conceptual framework for dislocation mechanics in ceramics, *Int. J. Ceram. Eng. Sci.*, 2022, **4**, 214–239, DOI: 10.1002/ces2.10150.

3 X. Fang, K. Ding, S. Janocha, C. Minnert, W. Rheinheimer, T. Frömling, K. Durst, A. Nakamura and J. Rödel, Nanoscale to microscale reversal in room-temperature plasticity in SrTiO3 by tuning defect concentration, *Scr. Mater.*, 2020, **188**, 228–232, DOI: 10.1016/j.scriptamat.2020.07.033.

4 L. Porz, A. J. Klomp, X. Fang, N. Li, C. Yildirim, C. Detlefs, E. Bruder, M. Höfling, W. Rheinheimer, E. A. Patterson, P. Gao, K. Durst, A. Nakamura, K. Albe, H. Simons, J. Rödel and L. Porz, Dislocation-toughened ceramics, *Mater. Horiz.*, 2021, **8**, 1528–1537, DOI: 10.1039/d0mh02033h.

5 B. Yang, P. E. Sánchez-Jiménez, T. Niu, T. Sun, Z. Shang, J. Cho, A. Perejón, C. Shen, L. A. Pérez-Maqueda, T. Tsakalakos, H. Wang and X. Zhang, In situ study on enhanced plastic deformability of Lanthanum-doped Bismuth ferrite processed by flash sintering, *J. Eur. Ceram. Soc.*, 2024, **44**, 3985–3994, DOI: 10.1016/j.jeurceramsoc.2023.12.099.

6 W. Rheinheimer, X. L. Phuah, L. Porz, M. Scherer, J. Cho and H. Wang, The impact of flash sintering on densification and plasticity of strontium titanate: high heating rates, dislocation nucleation and plastic flow, *J. Eur. Ceram. Soc.*, 2023, **43**, 3524–3537, DOI: 10.1016/j.jeurceramsoc.2023.02.007.

7 X. L. Phuah, J. Cho, T. Tsakalakos, A. K. Mukherjee, H. Wang and X. Zhang, Defects in flash-sintered ceramics and their effects on mechanical properties, *MRS Bull.*, 2021, **46**, 44–51, DOI: 10.1557/s43577-020-00014-y.

8 B. Yang, Z. Shang, J. Li, X. L. Phuah, J. Cho, H. Wang and X. Zhang, Effects of electric field on microstructure evolution and defect formation in flash-sintered TiO2, *J. Eur. Ceram. Soc.*, 2022, **42**, 6040–6047, DOI: 10.1016/j.jeurceramsoc.2022.06.009.

9 J. Cho, X. L. Phuah, J. Li, Z. Shang, H. Wang, H. Charalambous, T. Tsakalakos, A. K. Mukherjee, H. Wang and X. Zhang, Temperature effect on mechanical response of flash-sintered ZnO by *in situ* compression tests, *Acta Mater.*, 2020, **200**, 699–709, DOI: 10.1016/j.actamat.2020.09.029.

10 J. Cho, J. Li, H. Wang, Q. Li, Z. Fan, A. K. Mukherjee, W. Rheinheimer, H. Wang, X. Zhang and X. Zhang, Study of deformation mechanisms in flash-sintered yttria-stabilized zirconia by *in situ* micromechanical testing at elevated temperatures, *Mater. Res. Lett.*, 2019, **7**, 194–202, DOI: 10.1080/21663831.2019.1575924.

11 J. Li, J. Cho, J. Ding, H. Charalambous, S. Xue, H. Wang, X. L. Phuah, J. Jian, X. Wang, C. Ophus, T. Tsakalakos, R. Edwin García, A. K. Mukherjee, N. Bernstein, C. Stephen Hellberg, H. Wang and X. Zhang, Nanoscale stacking fault–assisted room temperature plasticity in flash-sintered TiO2, *Sci. Adv.*, 2019, **5**, eaaw5519, DOI: 10.1126/sciadv.aaw5519.

12 D. Brunner, S. Taeri-Baghbadrani, W. Sigle and M. Rühle, Surprising Results of a Study on the Plasticity in Strontium Titanate, *J. Am. Ceram. Soc.*, 2001, **84**, 1161–1163, DOI: 10.1111/j.1151-2916.2001.tb00805.x.

13 P. Gumbsch, S. Taeri-Baghbadrani, D. Brunner, W. Sigle and M. Rühle, *Plasticity and an Inverse Brittle-to-Ductile Transition in Strontium Titanate*, 2001. DOI: 10.1103/PhysRevLett.87.085505.

14 A. Montagne, V. Audurier and C. Tromas, Influence of pre-existing dislocations on the pop-in phenomenon during nanoindentation in MgO, *Acta Mater.*, 2013, **61**, 4778–4786, DOI: 10.1016/j.actamat.2013.05.004.

15 W. J. Moon, T. Ito, S. Uchimura and H. Saka, Toughening of ceramics by dislocation sub-boundaries, *Mater. Sci. Eng., A*, 2004, **387–389**, 837–839, DOI: 10.1016/j.msea.2004.01.133.

16 J. Amodeo, S. Merkel, C. Tromas, P. Carrez, S. Korte-Kerzel, P. Cordier and J. Chevalier, Dislocations and Plastic Deformation in MgO Crystals: A Review, *Crystals*, 2018, **8**, 240, DOI: 10.3390/cryst8060240.

17 L. Jin, X. Guo and C. L. Jia, TEM study of ⟨110⟩-type 35.26° dislocations specially induced by polishing of SrTiO3 single crystals, *Ultramicroscopy*, 2013, **134**, 77–85, DOI: 10.1016/j.ultramic.2013.06.009.

18 B. Yang, X. L. Phuah, Z. Shang, X. Sheng, H. Wang and X. Zhang, Effects of incubation on microstructure gradient in flash-sintered TiO2, *Scr. Mater.*, 2022, **207**, 114270, DOI: 10.1016/j.scriptamat.2021.114270.

19 M. Biesuz, L. Pinter, T. Saunders, M. Reece, J. Binner, V. M. Sglavo and S. Grasso, Investigation of Electrochemical, Optical and Thermal Effects during Flash Sintering of 8YSZ, *Materials*, 2018, **11**, 1214, DOI: 10.3390/ma11071214.

20 X. L. Phuah, B. Yang, H. Charalambous, T. Tsakalakos, X. Zhang and H. Wang, Microstructure and defect gradients in DC and AC flash sintered ZnO, *Ceram. Int.*, 2021, **47**, 28596–28602, DOI: 10.1016/j.ceramint.2021.07.018.

21 A. Uehashi, K. Sasaki, T. Tokunaga, H. Yoshida and T. Yamamoto, Formation of secondary phase at grain boundary of flash-sintered BaTiO3, *Microscopy*, 2014, **63**, i19–i20, DOI: 10.1093/jmicro/dfu048.

22 A. Uehashi, H. Yoshida, T. Tokunaga, K. Sasaki and T. Yamamoto, Enhancement of sintering rates in BaTiO3 by controlling of DC electric current, *J. Ceram. Soc. Jpn.*, 2015, **123**, 465–468, DOI: 10.2109/jcersj2.123.465.

23 H. Wang, X. L. Phuah, H. Charalambous, S. K. Jha, J. Li, T. Tsakalakos, X. Zhang and H. Wang, Staged microstructural study of flash sintered titania, *Materialia*, 2019, **8**, 100451, DOI: 10.1016/J.MTLA.2019.100451.

24 A. Karakuscu, M. Cologna, D. Yarotski, J. Won, J. S. C. Francis, R. Raj and B. P. Uberuaga, Defect Structure of Flash-Sintered Strontium Titanate, *J. Am. Ceram. Soc.*, 2012, **95**, 2531–2536, DOI: 10.1111/j.1551-2916.2012.05240.x.

25 S. Takeuchi and T. Hashimoto, *Deformation mechanisms in titanium dioxide single crystals*, 1990.

26 S. K. Jha, H. Charalambous, H. Wang, X. L. Phuah, C. Mead, J. Okasinski, H. Wang and T. Tsakalakos, *In situ* observation of oxygen mobility and abnormal lattice expansion in ceria during flash sintering, *Ceram. Int.*, 2018, **44**, 15362–15369, DOI: 10.1016/J.CERAMINT.2018.05.186.

27 J. C. M'Peko, J. S. C. Francis and R. Raj, Field-assisted sintering of undoped BaTiO3: Microstructure evolution and dielectric permittivity, *J. Eur. Ceram. Soc.*, 2014, **34**, 3655–3660, DOI: 10.1016/j.jeurceramsoc.2014.04.041.

28 W. Rheinheimer, X. L. Phuah, H. Wang, F. Lemke, M. J. Hoffmann and H. Wang, The role of point defects and defect gradients in flash sintering of perovskite oxides, *Acta Mater.*, 2019, **165**, 398–408, DOI: 10.1016/J.ACTAMAT.2018.12.007.

29 M. Biesuz and V. M. Sglavo, Current-induced abnormal and oriented grain growth in corundum upon flash sintering, *Scr. Mater.*, 2018, **150**, 82–86, DOI: 10.1016/j.scriptamat.2018.03.004.

30 C. Dellacorte and D. L. Deadmore, *Vickers indentation hardness of stoichiometric and reduced single crystal TiO_2 (rutile) from 25 to 800 °C*, NASA Technical Memorandum 105959, 1993.

31 M. Division, C. Electricity and G. Board, Stacking faults and dislocations in titanium dioxide, with special reference to non-stoichiometry, *Proc. R. Soc. London, Ser. A*, 1963, **276**, 542–552, DOI: 10.1098/rspa.1963.0225.

32 K. H. G. Ashbee and R. E. Smallman, The plastic deformation of titanium dioxide single crystals, *Proc. R. Soc. London, Ser. A*, 1963, **274**, 195–205, DOI: 10.1098/rspa.1963.0123.

33 S. Stich, K. Ding, Q. K. Muhammad, L. Porz, C. Minnert, W. Rheinheimer, K. Durst, J. Rödel, T. Frömling and X. Fang, Room-temperature dislocation plasticity in SrTiO3 tuned by defect chemistry, *J. Am. Ceram. Soc.*, 2022, **105**, 1318–1329, DOI: 10.1111/jace.18118.

34 G. A. Illarionov, S. M. Morozova, V. V. Chrishtop, M. A. Einarsrud and M. I. Morozov, Memristive TiO2: Synthesis, Technologies, and Applications, *Front. Chem.*, 2020, **8**, 724, DOI: 10.3389/fchem.2020.00724.

35 Nanotechnology TiO 2-a prototypical memristive material Related content Cluster-like resistive switching of SrTiO 3 : Nb surface layers-Nanofilamentary resistive switching in binary oxide system; a review on the present statusand outlook-Emerging memories: resistive switching mechanisms and current status-Recent citations, 2011. DOI: 10.1088/0957-4484/22/25/254001.

36 D. H. Kwon, K. M. Kim, J. H. Jang, J. M. Jeon, M. H. Lee, G. H. Kim, X. S. Li, G. S. Park, B. Lee, S. Han, M. Kim and C. S. Hwang, Atomic structure of conducting nanofilaments in TiO2 resistive switching memory, *Nat. Nanotechnol.*, 2010, **5**, 148–153, DOI: 10.1038/nnano.2009.456.

37 S. Abdelouahed and K. P. McKenna, Relevance of non-equilibrium defect generation processes to resistive switching in TiO2, *J. Appl. Phys.*, 2015, **118**, 134103, DOI: 10.1063/1.4932225.

38 R. Katal, M. Salehi, M. H. Davood Abadi Farahani, S. Masudy-Panah, S. L. Ong and J. Hu, Preparation of a New Type of Black TiO2 under a Vacuum Atmosphere for Sunlight Photocatalysis, *ACS Appl. Mater. Interfaces*, 2018, **10**, 35316–35326, DOI: 10.1021/acsami.8b14680.

39 A. Naldoni, M. Altomare, G. Zoppellaro, N. Liu, Š. Kment, R. Zbořil and P. Schmuki, Photocatalysis with reduced TiO 2 : From Black TiO 2 to cocatalyst-free hydrogen production, *ACS Catal.*, 2019, **9**, 345–364, DOI: 10.1021/acscatal.8b04068.

40 A. Sinhamahapatra, J.-P. Jeon and J.-S. Yu, *Oxygen-deficient Reduced TiO 2-X : Surface Properties and Photocatalytic Activity*, 2015.

41 S. Chen, Y. Xiao, Y. Wang, Z. Hu, H. Zhao and W. Xie, A facile approach to prepare black TiO2 with oxygen vacancy for enhancing photocatalytic activity, *Nanomaterials*, 2018, **8**, 245, DOI: 10.3390/nano8040245.

42 H. Tan, Z. Zhao, M. Niu, C. Mao, D. Cao, D. Cheng, P. Feng and Z. Sun, A facile and versatile method for preparation of colored TiO2 with enhanced solar-driven photocatalytic activity, *Nanoscale*, 2014, **6**, 10216–10223, DOI: 10.1039/c4nr02677b.

43 F. C. Walsh and R. G. A. Wills, The continuing development of Magnéli phase titanium sub-oxides and Ebonex® electrodes, *Electrochim. Acta*, 2010, **55**, 6342–6351, DOI: 10.1016/j.electacta.2010.05.011.

44 J. Ye, G. Wang, X. Li, Y. Liu and R. Zhu, Temperature effect on electrochemical properties of Ti4O7 electrodes prepared by spark plasma sintering, *J. Mater. Sci.: Mater. Electron.*, 2015, **26**, 4683–4690, DOI: 10.1007/s10854-015-2838-1.

45 J. R. Smith, F. C. Walsh and R. L. Clarke, Electrodes based on Magnéli phase titanium oxides: the properties and applications of Ebonex® materials, *J. Appl. Electrochem.*, 1998, **28**, 1021–1033, DOI: 10.1023/A:1003469427858.

46 Y. Bai, I. Mora-Seró, F. De Angelis, J. Bisquert and P. Wang, Titanium Dioxide Nanomaterials for Photovoltaic Applications, *Chem. Rev.*, 2014, **114**, 10095–10130, DOI: 10.1021/cr400606n.

47 R. L. Clarke and S. K. Harnsberger, New electrically conductive ceramic–a fundamental advance in electrode technology, *Am. Lab.*, 1988, **20**, 8.

48 Y. Dang and A. R. West, Oxygen stoichiometry, chemical expansion or contraction, and electrical properties of rutile, TiO2±δ ceramics, *J. Am. Ceram. Soc.*, 2019, **102**, 251–259, DOI: 10.1111/jace.15889.

49 R. Sun, Z. Wang, M. Saito, N. Shibata and Y. Ikuhara, Atomistic mechanisms of nonstoichiometry-induced twin

boundary structural transformation in titanium dioxide, *Nat. Commun.*, 2015, **6**, 2–4, DOI: **10.1038/ncomms8120**.

50 X. Wu, N. Yang, Y. Ji, X. He, Q. Li, R. Jiang, Z. Lei, Z. Liu and J. Sun, Phase transformation and interface crystallography between TiO2 and different TinO2n −1 phases, *CrystEngComm*, 2023, DOI: **10.1039/d2ce01410f**.

51 J. Kwon, A. A. Sharma, J. A. Bain, Y. N. Picard and M. Skowronski, Oxygen vacancy creation, drift, and aggregation in TiO_2-based resistive switches at low temperature and voltage, *Adv. Funct. Mater.*, 2015, **25**, 2876–2883, DOI: **10.1002/adfm.201500444**.

52 A. Moballegh and E. C. Dickey, Electric-field-induced point defect redistribution in single-crystal TiO2-x and effects on electrical transport, *Acta Mater.*, 2015, **86**, 352–360, DOI: **10.1016/j.actamat.2014.11.032**.

53 Y. Motohashi, M. G. Blanchin, E. Vicario, G. Fontaine and S. Otake, Elastic Parameters, Elastic Energy, and, Stress Fields of Dislocations in TiO_2 Rutile Crystals, *Phys. Status Solidi A*, 1979, **54**, 355–364, DOI: **10.1002/pssa.2210540144**.

54 S. Harada, K. Tanaka and H. Inui, Thermoelectric properties and crystallographic shear structures in titanium oxides of the Magnèli phases, *J. Appl. Phys.*, 2010, **108**, 083703, DOI: **10.1063/1.3498801**.

55 X. Fang, H. Bishara, K. Ding, H. Tsybenko, L. Porz, M. Höfling, E. Bruder, Y. Li, G. Dehm and K. Durst, Nanoindentation pop-in in oxides at room temperature: Dislocation activation or crack formation?, *J. Am. Ceram. Soc.*, 2021, **104**, 4728–4741, DOI: **10.1111/jace.17806**.

56 W. C. Oliver and G. M. Pharr, *An improved technique for determining hardness and elastic modulus using load and displacement sensing indentation experiments*, 1992.

57 D. B. Williams and C. B. Carter, *Transmission electron microscopy: a textbook for materials science*, Springer, 2009.

58 T. W. Butler, *On the determination of dislocation densities*, 1969. DOI: **10.1080/03071845709423438**.

59 X. Tian, C. Cook, W. Hong, T. Ma, G. L. Brennecka and X. Tan, In Situ TEM Study of the Amorphous-to-Crystalline Transition during Dielectric Breakdown in TiO_2 Film, *ACS Appl. Mater. Interfaces*, 2019, **11**, 40726–40733, DOI: **10.1021/acsami.9b08146**.

60 F. Wang, R. Shi, Y. Lei, Z. Lei, R. Jiang, D. Wang, Z. Liu and J. Sun, Formation mechanisms of interfaces between different TiNO2n-1 phases prepared by carbothermal reduction reaction, *CrystEngComm*, 2019, **21**, 524–534, DOI: **10.1039/c8ce01459k**.

61 J. A. Zimmerman, C. L. Kelchner, P. A. Klein, J. C. Hamilton and S. M. Foiles, Surface Step Effects on Nanoindentation, *Phys. Rev. Lett.*, 2001, **87**, 165507, DOI: **10.1103/PhysRevLett.87.165507**.

62 A. Gouldstone, H.-J. Koh, K.-Y. Zeng, A. E. Giannakopoulos and S. Suresh, Discrete and continuous deformation during nanoindentation of thin films, *Acta Mater.*, 2000, **48**, 2277–2295, DOI: **10.1016/S1359-6454(00)00009-4**.

63 S. A. Syed Asif and J. B. Pethica, Nanoindentation creep of single-crystal tungsten and gallium arsenide, *Philos. Mag. A*, 1997, **76**, 1105–1118, DOI: **10.1080/01418619708214217**.

64 S. Jayashree and M. Ashokkumar, Switchable intrinsic defect chemistry of titania for catalytic applications, *Catalysts*, 2018, **8**, 601, DOI: **10.3390/catal8120601**.

65 G. Cheng, C. Miao, Q. Qin, J. Li, F. Xu, H. Haftbaradaran, E. C. Dickey, H. Gao and Y. Zhu, Large anelasticity and associated energy dissipation in single-crystalline nanowires, *Nat. Nanotechnol.*, 2015, **10**, 687–691, DOI: **10.1038/nnano.2015.135**.

66 L. Li, G. Chen, H. Zheng, W. Meng, S. Jia, L. Zhao, P. Zhao, Y. Zhang, S. Huang, T. Huang and J. Wang, Room-temperature oxygen vacancy migration induced reversible phase transformation during the anelastic deformation in CuO, *Nat. Commun.*, 2021, **12**, 3863, DOI: **10.1038/s41467-021-24155-z**.

67 J. Pelleg, The Strength and Strengthening of Ceramics, *Mechanical Properties of Ceramics*, Springer International Publishing, Cham, 2014, pp. 351–415. DOI: **10.1007/978-3-319-04492-7_5**.